www.pss-rapid.com

Low Resistivity Sputter Deposited SnO_x Thin Films: An Indium-Free Transparent Conductive Oxide?

Marlene Härtel, Angelika Harter, Darja Erfurt, Reiner Klenk, Alexander Steigert, Lars Korte, Rutger Schlatmann, and Bernd Stannowski*

This study investigates the influence of oxygen concentration and thermal treatment on the optical and electrical properties of tin oxide (SnO_x) thin films deposited via radio frequency (RF) magnetron sputtering. The oxygen content in the sputtering process gas is systematically varied, revealing its critical role in influencing the films' charge carrier density, mobility, and resistivity. Optimal conductivity (resistivity as low as 3.4 mΩ cm) is achieved at an argon-oxygen mix gas flow rate of 3.4 sccm combined with quasi-in-situ heating, enhancing both charge carrier density and mobility. Optical analysis revealed that transmittance and absorptance depend on oxygen flow. In the long-wavelength range, absorption scales with the number of free carriers, while in the short-wavelength range, discrete absorption peaks below the band gap were observed, possibly originating from a secondary SnO-like phase.

1. Introduction

Transparent conductive oxides (TCOs) are used in various opto-electrical applications. The most commonly used TCOs, due to their outstanding conductivity and high transparency, are indium-based, such as indium tin oxide (ITO) or indium zinc oxide (IZO). These TCOs achieve resistivities (ρ) of less than 1 mΩ cm with transparencies of over 80% in the ultraviolet-visible-near-infrared (UV-VIS-NIR) light spectrum.[1] However, indium is a scarce element whose demand is growing with the need for optoelectrical devices, which will lead to supply problems in the long term and will probably further increase the price of this resource, making it unattractive for large-scale production.[2] The task of researching alternative materials in order to achieve equally good TCOs that are not indium-based is, therefore, extremely important. One potential candidate for this goal is Tin. Tin oxide (SnO_x) is a wide-band gap metal oxide that has outstanding optical properties and obtains its conductivity via intrinsic or extrinsic doping.[3,4] As an example, high temperature (>500 °C) chemical vapor deposited fluorine-doped tin oxide (SnO_x:F, FTO) on glass is already a commercially widely used TCO for thin-film PV modules. For deposition on temperature-sensitive devices, such as silicon-heterojunction or metal-halide perovskite-based solar cells, temperatures need to be limited to max. 100–200 °C. Typical fabrication processes of SnO_x layers are atomic layer deposition,[5–7] magnetron sputtering,[8–13] pulsed laser deposition,[14,15] or reactive plasma deposition,[16] to name a few. Sputtering and reactive plasma deposition, in particular, have been used to explore this TCO alternative with the goal of an indium-free electrode, presumably because they offer a large window of process parameter variation to optimize for conductivity. In the case of non-extrinsically doped SnO_x, undercoordinated Sn atoms and oxygen vacancies are considered charge carrier donors.[3,11,16] Recently, Koida et al. presented SnO_x films deposited by reactive plasma deposition with charge carrier densities (N_e) of up to 1.8×10^{20} cm^{-3} and ρ as low as 1.3 mΩ cm with non-intentionally heated ("cold") deposition conditions. After post-annealing at 200 °C of the same films, N_e was increased to 2.7×10^{20} cm^{-3} with ρ lower than 1 mΩ cm.[16] **Table 1** provides an overview of the properties of SnO_x films achieved in earlier publications compared to properties achieved in this work. According to this literature review, one of the highest N_e was achieved for a sputter-deposited SnO_x film at low temperatures. Please note that the values compared in this table do not necessarily belong to films with the lowest ρ of the respective study but to films with the highest achieved N_e. Furthermore, the potential for improving the SnO_x film even further is shown by adding heat during the deposition. With that approach, a SnO_x film resistivity of 3.4 mΩ cm was achieved.

In this work, the optoelectrical behavior and structure of SnO_x films prepared by radio frequency (RF) magnetron sputtering are analyzed by systematically varying the oxygen content in the process gas mixture and applying several temperature treatments. The process gas consists of two contributions—a pure argon

M. Härtel, A. Harter, D. Erfurt, R. Klenk, A. Steigert, R. Schlatmann, B. Stannowski
Competence Centre Photovoltaics Berlin
Helmholtz-Zentrum Berlin für Materialien und Energie GmbH
12489 Berlin, Germany
E-mail: marlene.haertel@helmholtz-berlin.de

L. Korte
Department Perovskite Tandem Solar Cells
Helmholtz-Zentrum Berlin für Materialien und Energie GmbH
12489 Berlin, Germany

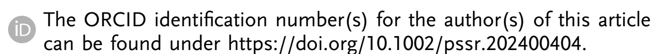
The ORCID identification number(s) for the author(s) of this article can be found under https://doi.org/10.1002/pssr.202400404.

© 2025 The Author(s). physica status solidi (RRL) Rapid Research Letters published by Wiley-VCH GmbH. This is an open access article under the terms of the Creative Commons Attribution License, which permits use, distribution and reproduction in any medium, provided the original work is properly cited.

DOI: 10.1002/pssr.202400404

18626270, 0, Downloaded from https://onlinelibrary.wiley.com/doi/10.1002/pssr.202400404 by Helmholtz-Zentrum Berlin Für, Wiley Online Library on [02/03/2025]. See the Terms and Conditions (https://onlinelibrary.wiley.com/terms-and-conditions) on Wiley Online Library for rules of use; OA articles are governed by the applicable Creative Commons License

Table 1. Overview of depositions method, highest achieved ne, hall mobility (μ_H), ρ, thickness (d), and reference (ref.) for SnO_x films deposited at moderate temperatures in previous publications.

Deposition method	N_e [$\times 10^{20}$ cm^{-3}]	μ_H [cm^2 Vs^{-1}]	ρ [mΩ cm]	d [nm]	References
Reactive RF magnetron sputtering at 100 °C	0.7	20.7	4.5		[31]
magnetron sputtering no intentional heating	1.29	8.00	5.6	99	[12]
Reactive RF magnetron sputtering at room temp.	1.41	12.11	3.7	285	[18]
RPD no intentional heating	1.8	25	1.3	<100	[16]
This work no intentional heating	1.5	7.7	5.3	92	–
This work "in-situ" 150 °C	1.7	11.1	3.4	89	–

(Ar) source and an argon-oxygen (ArO_2) mix gas source, with a ratio of Ar:O_2 of 97.5:2.5%. The oxygen content variation was achieved by changing the ArO_2 flow rate from 2.8 to 8 sccm, while the pure Ar flow rate was kept constant at 45 sccm.

The sputter deposition was carried out in a von Ardenne CS520s at a power density of 0.8 W cm^{-1} (100 W applied power to a 5-inch round, planar target) using a ceramic SnO_2 target that was manufactured with a purity of 99.99%. Post-annealing was performed following the deposition using a heating plate in the air at 130 or 210 °C for 10 min. Quasi-in-situ sample heating was carried out at a pretreatment station in the sputtering process chamber at 150 °C for 10 min. For that, the sample was moved to the position of the radiative heater before or after the sputter coating. 1.1-mm thick Corning glasses were used as substrates.

The IZO film was sputter deposited via RF magnetron sputtering in a Roth & Rau MicroSys 200 PVD system on a quartz glass substrate. The target used had a size of 2 inches and a composition of 90 wt% In_2O_3 and 10 wt% ZnO (purchased from FHR Anlagenbau GmbH). The RF power density was 4.21 W cm^{-2}, and the oxygen content in the process gas was 0.25%.

The coating thicknesses were determined using RT measurement and fitting the spectra with a Lorentz-Drude model. The electrical properties ρ, N_e, and μ_η were determined from Hall effect measurements with Van der Pauw geometry at a constant magnetic field of 0.56 T at room temperature. The optical behavior was measured with a UV-VIS-NIR double-beam Perkin Elmer Lambda - 1050 spectrophotometer in the wavelength range from 250 to 2450 nm. The film structure was analyzed by X-ray diffraction with the CuKα line.

2. Results

2.1. Screening of Added Oxygen Ratio during the RF Sputter Deposition

The conductivity of n-type TCOs is usually achieved by high doping with electron donors; in the case of tin oxide, oxygen vacancies, and undercoordinated Sn cations could be sources of free charge carriers.[16,17] During thin film fabrication, the oxygen vacancies that is the amount of oxygen incorporated in the film, can be influenced relatively easily by controlling the amount of added oxygen during the sputter deposition process. With this in mind, an experiment was carried out in which the oxygen content in the process gas was varied systematically in order to adjust the stoichiometry of the sputter-deposited SnO_x layers precisely and to investigate the effects on the electrical and optical properties of the resulting thin films. For this purpose, Hall measurements and spectrophotometry measurements were carried out, and the respective results are visualized in **Figure 1**a–c.

Both the electrical and optical properties of the SnO_x films show a clear dependence on the oxygen content in the process gas.

N_e reaches a value of 1.3×10^{20} cm^{-3} at the lowest tested ArO_2 flow rate of 2.8 sccm, increases to 1.5×10^{20} cm^{-3} for ArO_2 flow rates in the range of 3–3.6 sccm, and decreases for higher ArO_2 flow rates from 1.4×10^{20} cm^{-3} at 4 sccm ArO_2 flow to values $<1 \times 10^{20}$ cm^{-3} for ArO_2 flow rates >5 sccm. At 8 sccm ArO_2 flow, N_e reaches the lowest observed value of 0.6×10^{20} cm^{-3}. μ_H initially rises from 6.7 cm^2 Vs^{-1} at 2.8 sccm ArO_2 flow to a maximum of 8.2 cm^2 Vs^{-1} at 4 sccm before decreasing for higher ArO_2 rates of 5, 6, and 8 sccm to 7.0, 6.3 and 3.5 cm^2 Vs^{-1}, respectively. These values can be found in Figure 1a as well as in **Table 2**.

It can be noted that the relationship between electrical properties and oxygen content is not linear. ρ reaches a minimum of 5.3 mΩ cm at 3.4 sccm ArO_2 flow, which roughly corresponds to the maxima of N_e and μ_H (at 3.4 sccm: 1.5×10^{20} cm^{-3} and 7.7 cm^2 Vs^{-1}), and is higher for both less and more oxygen content in the process gas. In fact, the highest measured value for μ_H is 8.2 cm^2 Vs^{-1} at 4 sccm oxygen flow and, therefore, is slightly higher than for the 3.4 sccm films. However, the lower N_e of 1.4×10^{20} cm^{-3} dominates the equation for the resistivity $\rho = R_{sheet} \cdot d = (N_e \cdot \mu_H \cdot e)^{-1}$, which leads to a slightly higher value.

The influence of varying oxygen amounts in the process gas during film fabrication on the optical properties of the thin film is shown in Figure 1b,c. In particular, the optics in the long-wavelength range for wavelengths above 1000 nm show a strong dependence on the oxygen content. The transmittance in this range increases gradually with the oxygen flow, and the higher the wavelength, the greater the increase. At 2400 nm, the transmittance increases by 20% over the observed range, from ≈67% for 2.6 sccm ArO_2 flow to ≈87% for 8 sccm ArO_2 flow. This increase in transmittance with increasing oxygen content in the process gas clearly correlates with the reduction in absorptance in the same spectral range, while the reflectance hardly changes in this range. In fact, it can even be observed that for films deposited at 5 sccm ArO_2 or more, the reflectance increases slightly. For an ArO_2 flow of 8 sccm the reflectance for that range increases by ≈3% in the range from 1000 to 2200 nm compared to the reflectance of films fabricated at 4 sccm ArO_2 or less.

© 2025 The Author(s). physica status solidi (RRL) Rapid Research Letters published by Wiley-VCH GmbH

18626270, 0, Downloaded from https://onlinelibrary.wiley.com/doi/10.1002/pssr.202400404 by Helmholtz-Zentrum Berlin Für, Wiley Online Library on [02/03/2025]. See the Terms and Conditions (https://onlinelibrary.wiley.com/terms-and-conditions) on Wiley Online Library for rules of use; OA articles are governed by the applicable Creative Commons License

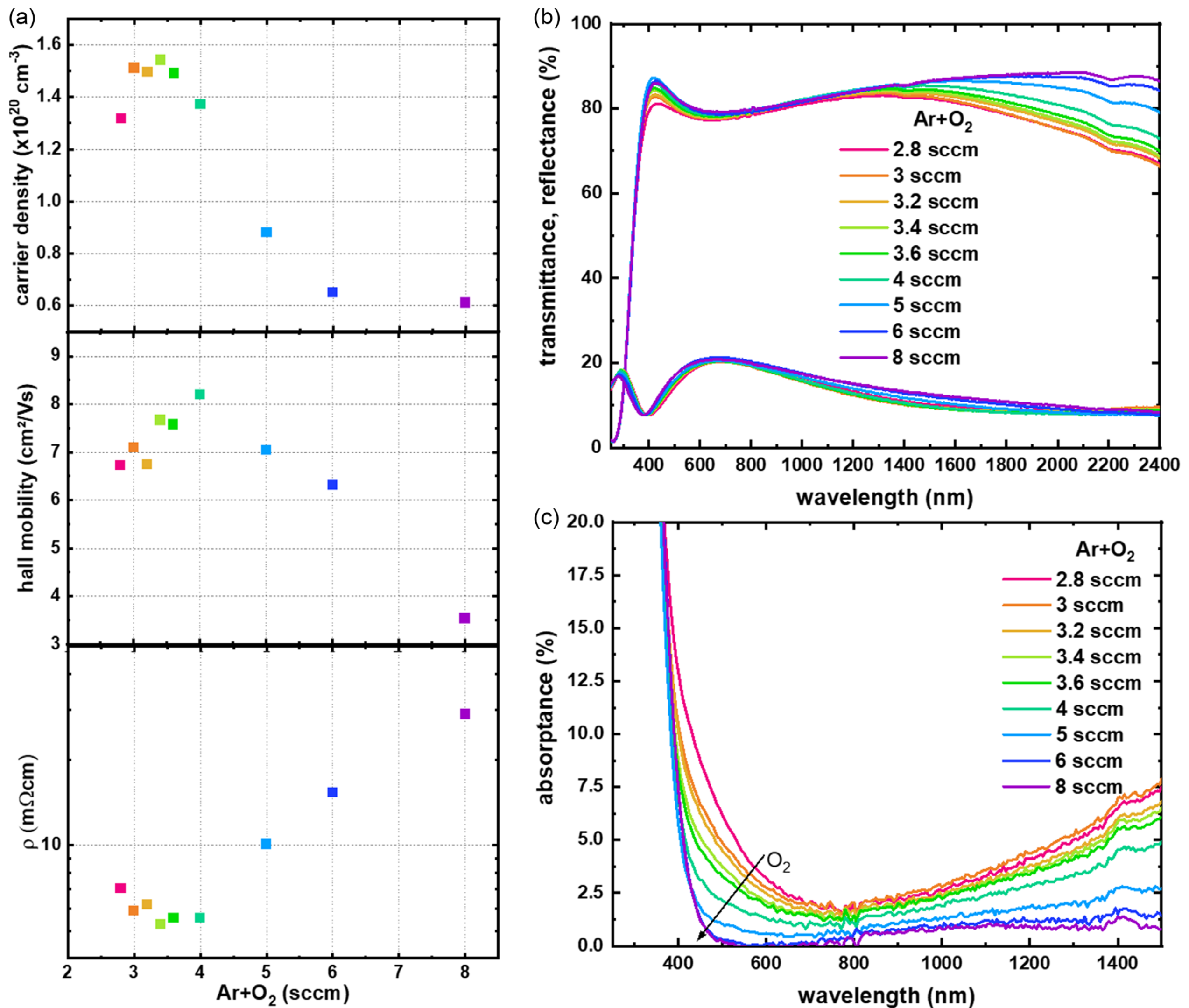

Figure 1. Results of the oxygen variation of SnO_x thin films deposited on corning glass with regard to the a) electrical properties represented by carrier density (N_e), mobility (μ_H), and resistivity (ρ), and b,c) optical properties, displaying the transmittance and reflectance, and the thereof calculated absorptance, respectively.

Table 2. Electrical parameters and film properties of SnO_x thin films, at the corresponding ArO_2 flow rates.

ArO_2 flow [sccm]	N_e [$\times 10^{20}$ cm^{-3}]	μ_H [cm^2 Vs^{-1}]	ρ [mΩ cm]	d [nm]	E_g [eV]	E_U [meV]
2.8	1.3	6.7	7.1	92	3.3	621
3	1.5	7.1	5.9	92	3.3	703
3.2	1.5	6.8	6.2	92	3.3	711
3.4	1.5	7.7	5.3	92	3.3	713
3.6	1.5	7.6	5.5	91	3.3	770
4	1.4	8.2	5.6	90	3.3	858
5	0.9	7.0	10.1	92	3.3	695
6	0.7	6.3	15.3	87	3.2	187
8	0.6	3.5	28.9	87	3.2	161

For wavelengths below 800 nm, a further dependence of the absorption on the oxygen content can be observed, which is shown in Figure 1c. Here, too, the absorption gradually decreases with increasing oxygen content in the process gas. The change in absorption in this wavelength range can generally be explained by two mechanisms. Either it is due to a change in band-to-band absorption, that is absorption of photons with an energy corresponding to the optical band gap of the material, which would correspond to a change in the optical band gap (E_g), or a change in sub-band absorption for example via band-tail states within the band gap, so-called Urbach tails. We plotted the absorption coefficient (α) in a semi-logarithmic scale and $(\alpha E)^{1/2}$ as a function of photon energy (E_{ph}) (see Figure 3a,b), which reveals that the band gap absorption shifts only a little depending on the tested ArO_2 flow range, but the sub-band gap absorption, often quantified by the Urbach energy (E_U),

© 2025 The Author(s). physica status solidi (RRL) Rapid Research Letters published by Wiley-VCH GmbH

exhibits a strong dependence on the oxygen content. The values extracted by linear fittings for E_g ($(\alpha E_{ph})^{1/2} \propto E_{ph}$) and the Urbach energy, calculated following the Urbach relation $\alpha(E_{ph}) = \alpha_0 \cdot \exp(-E_{ph}/E_U)$, can be found in Table 2. The calculated E_g values for all films fabricated of ArO_2 flow rates between 2.8 and 5 sccm is 3.3 eV, and for higher ArO_2 flows of 6 and 8 sccm, E_g seems to shift to lower energies according to **Figure 2**b) slightly and is calculated to be ≈3.2 eV. As already seen from the absorption coefficient in **Figure 3**a), the sub-band gap absorption shows a strong dependency on the ArO_2 flow rate. From 2.8 sccm ArO_2 to 4 sccm ArO_2, the calculated E_U increases gradually from 621 to 858 meV. At 5 sccm ArO_2, E_U first decreases slightly to 695 meV, and at 6 and 8 sccm ArO_2 E_U decreases dramatically to 187 and 161 meV, respectively. Interestingly, this trend is roughly the same for μ_H.

2.2. Different Temperature Treatments during and after Sputter Deposition

Thermal post-annealing is a commonly used method to modify the electrical and optical properties of TCOs, such as ITO. Often higher conductivities can be achieved by reducing defects, thermal activation, and stimulating crystallization.[13,18,19] Depending on the application, however, the underlying layer system sets thermal limits. For example, metal-halide perovskite-based solar cells can withstand temperatures of only up to 130–150 °C for a short time,[20] and silicon heterojunction solar cells are typically treated with temperatures of up to 210 °C.[21,22] Post-annealing treatments of 10 min in air and temperatures of 130 and 210 °C were thus tested for the SnO_x layers with the lowest resistivity from the test series in Section A). In addition, two quasi-in-situ heating options were investigated in the sputtering chamber for the same process conditions. Firstly, the substrate was preheated at 150 °C for 10 min directly before coating, and secondly, the substrate was preheated and post-heated at 150 °C for 10 min each. Optically, the films prepared at 3.4 sccm ArO_2 flow rate and which have received no or different temperature treatments do not differ as significantly as under varying oxygen flow rates (see Figure 3). Nevertheless, a slight trend for transmittance and absorptance in the long wavelength range can be observed. While in this range, layers that have received an in-situ pre- and post-heating show a slight increase in absorptance and reduction in transmittance, as well as a reduction in reflectance between 800 and 2000 nm, compared to the 3.4 sccm as-deposited layer, an opposite trend is observed for all other temperature treatments for transmittance and absorptance beyond 1000 nm. Both the in-situ pre-treatment at 150 °C and the post-annealing at 130 and 210 °C lead to a slight reduction in absorptance and an increase in transmission in the long wavelength range. A very similar trend can be observed for the charge carrier density (see **Table 3**). While the in-situ pre- and post-heating leads to an increase in charge carrier density to 1.7×10^{20} cm^{-3} compared to the unheated 3.4 sccm ArO_2 sample, which has a charge carrier density of 1.5×10^{20} cm^{-3}, the charge carrier density for all other temperature treatments drops to 1.4×10^{20} cm^{-3}.

The Hall mobilities of as-deposited, 130 °C post-annealed and 210 °C post-annealed SnO_x films prepared at 3.4 sccm ArO_2 flow rate are 7.7, 8.9 and 6.7 cm^2 Vs^{-1}, respectively. Significantly higher Hall mobilities were achieved by the in-situ temperature treatment. Pre-treatment at 150 °C resulted in Hall mobilities of 10.1 cm^2 Vs^{-1} for films produced at 3.4 sccm ArO_2 flow rate, and pre- and post-heating resulted in Hall mobilities of 11.1 cm^2 Vs^{-1}. The ρ, which results from the charge carrier density and charge carrier mobility, follows these trends. It increases from 5.3 mΩ cm for the as-deposited SnO_x layers to 6.7 mΩ cm for 210 °C post-annealed SnO_x layers, while for the in-situ pre- and post-heating, it leads to the lowest ρ of this experiment of 3.4 mΩ cm.

Furthermore, E_U and E_g were calculated from linear fits of the absorption coefficient (α) and with the help of the Tauc plot by plotting $(\alpha h\nu)^{1/2}$ as a function of E_{ph} to investigate the impact of the temperature treatment on the absorptance for wavelengths <800 nm (Figure 3b–d). The calculated E_g exhibits no significant temperature treatment-depending change, while a slight shift of the absorption coefficient toward lower energies can be seen for films that were pre-treated at 150 °C (Figure 3c). For all films, E_g was calculated to be 3.3 eV. The absorptance changes for wavelengths <800 nm mainly stem from the small changes in the sub-gap absorption. The corresponding calculated values for

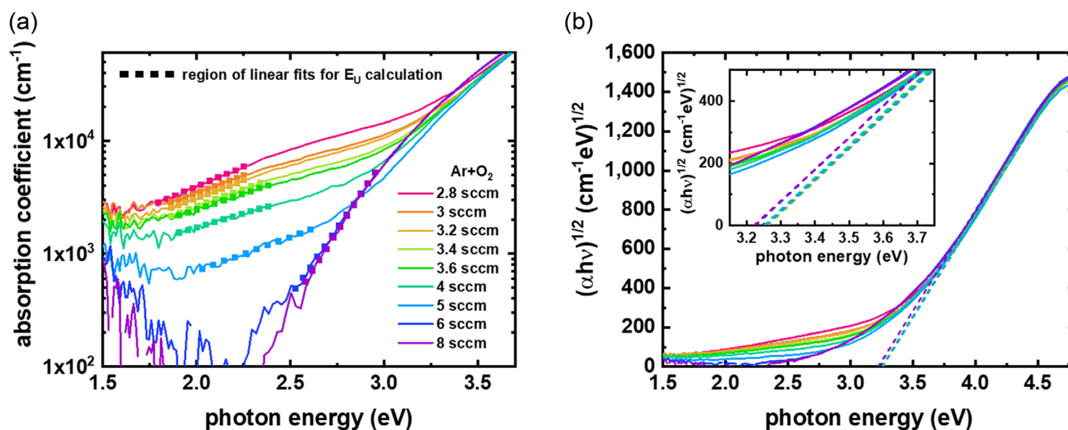

Figure 2. a) Absorption coefficient $\alpha(E_{ph})$ calculated as $\alpha(E_{ph}) = -1/d \cdot \ln(T(E_{ph})/(1-R(E_{ph}))$, and b) Tauc plot with an inset showing a zoomed-in view of the intersection region where the linear interpolation meets the x-axis. Data corresponds to SnO_x films deposited on glass under varying oxygen content.

© 2025 The Author(s). physica status solidi (RRL) Rapid Research Letters published by Wiley-VCH GmbH

18626270, 0, Downloaded from https://onlinelibrary.wiley.com/doi/10.1002/pssr.202400404 by Helmholtz-Zentrum Berlin Für, Wiley Online Library on [02/03/2025]. See the Terms and Conditions (https://onlinelibrary.wiley.com/terms-and-conditions) on Wiley Online Library for rules of use; OA articles are governed by the applicable Creative Commons License

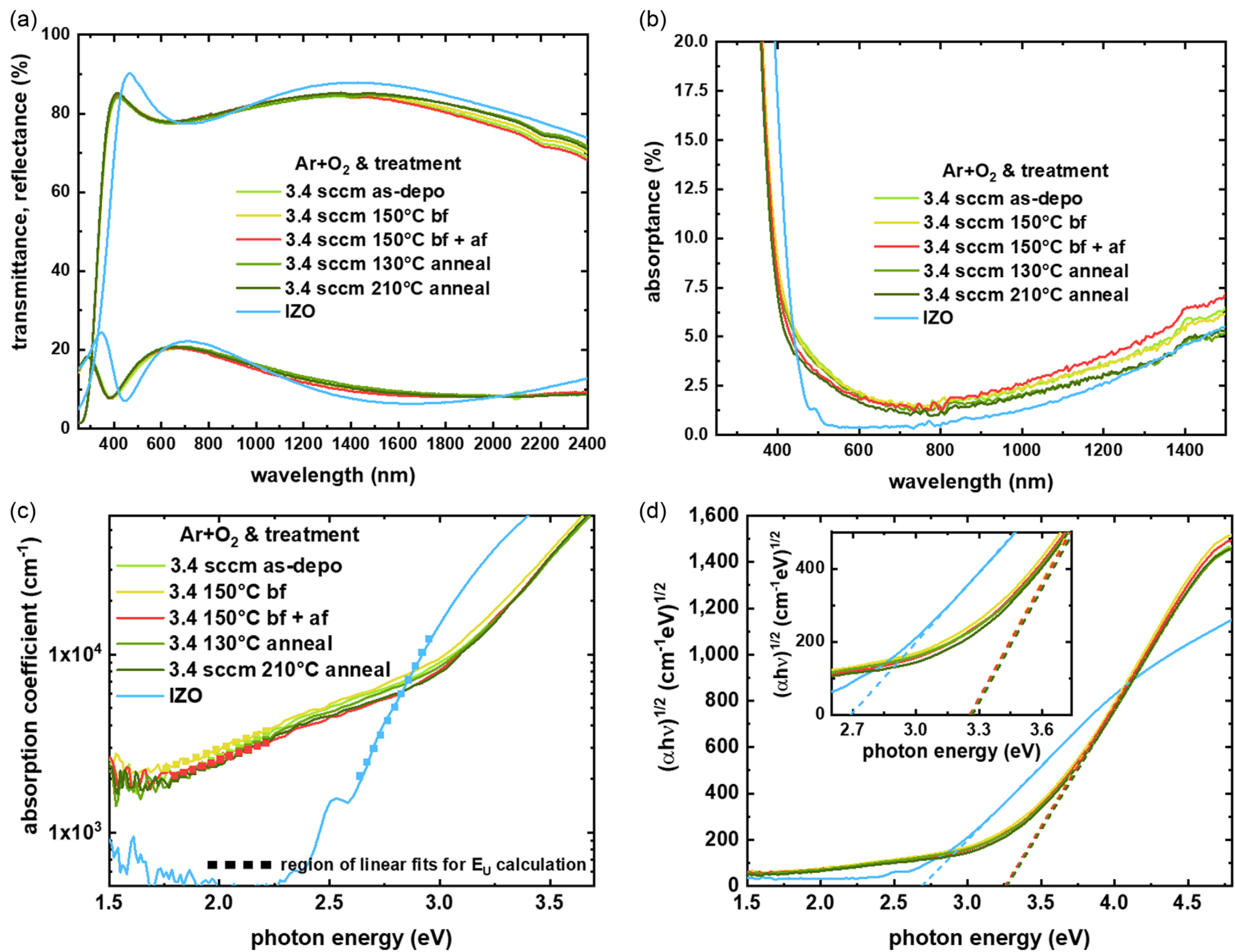

Figure 3. Optical properties of SnO_x films that received various heat treatments compared to a conventional IZO thin film (light blue), displaying a) the transmittance and reflectance, b) the thereof calculated absorptance, c) the absorption coefficient, and d) the Tauc plot with an inset showing a zoomed-in view of the intersection region where the linear interpolation meets the *x*-axis.

Table 3. Electrical parameters and film properties of SnO_x thin films, depending on various heat treatments and in comparison to a conventional IZO thin film.

	N_e [$\times10^{20}$ cm^{-3}]	μ_H [cm^2 Vs^{-1}]	ρ [mΩ cm]	d [nm]	E_g [eV]	E_U [meV]
3.4 sccm as-deposited	1.5	7.7	5.3	92	3.3	713
3.4 sccm 130 °C anneal	1.4	8.9	4.9	92	3.3	716
3.4 sccm 210 °C anneal	1.4	6.7	6.7	92	3.3	691
3.4 sccm 150 °C before (bf)	1.4	10.1	4.3	86	3.3	784
3.4 sccm 150 °C bf + after	1.7	11.1	3.4	89	3.3	821
IZO	2.9	49.5	0.4	100	2.7	167

the E_U can be found in Table 3. While annealing at 130 °C does not cause a significant change in E_U compared to as-deposited layers (716 and 713 meV, respectively), annealing at 210 °C leads to a reduction in E_U to 691 meV. On the other hand, the in-situ treatments at 150 °C led to a significant increase in E_U to 784 meV for the pre-treatment and 821 meV for the pre- and post-heating at 150 °C.

Compared to a conventional IZO film, which is often used as a transparent front electrode in solar cells, the SnO_x has a fundamentally similar optical behavior. However, the band gap

© 2025 The Author(s). physica status solidi (RRL) Rapid Research Letters published by Wiley-VCH GmbH

18626270, 0, Downloaded from https://onlinelibrary.wiley.com/doi/10.1002/pssr.202400404 by Helmholtz-Zentrum Berlin Für, Wiley Online Library on [02/03/2025]. See the Terms and Conditions (https://onlinelibrary.wiley.com/terms-and-conditions) on Wiley Online Library for rules of use; OA articles are governed by the applicable Creative Commons License

physica status solidi rrl
www.pss-rapid.com

absorption of IZO is shifted toward higher wavelengths, which equates to a smaller E_g, which is calculated here to be 2.7 eV. On the other hand, the sub-gap absorption between 500 and 800 nm is significantly lower for IZO than for the SnO_x films, which is well visible in Figure 3. The calculated Urbach energy for IZO is 167 meV—a value close to that of SnO_x at high ArO_2 flow rates. However, at 0.4 mΩ cm, the ρ of IZO is significantly lower than the best ρ achieved for SnO_x in this experiment, which is primarily due to a significantly higher N_e of 2.9×10^{20} cm^{-3} coupled with a significantly higher μ_H of 49.5 cm^2 Vs^{-1}.

3. Discussion

This study shows that the optical and electrical properties of SnO_x thin films deposited by RF magnetron sputtering from a ceramic SnO_2 target depend significantly on the oxygen content during sputter deposition, as well as on thermal treatments. With this optimization of the oxygen content in the process gas in a cold sputter deposition process, carrier densities as high as 1.5×10^{20} cm^{-3} were achieved, and by applying a pre- and post-heating step at 150 °C, N_e was increased to 1.7×10^{20} cm^{-3}, which is, to the best of our knowledge, amongst the highest reported N_e for SnO_x deposited by sputter deposition at low temperatures. Charge carrier donors in the case of SnO_x can be oxygen vacancies or undercoordinated Sn cations. The dependency of the free charge carriers in the SnO_x films on the oxygen content of the process gas in this experiment was demonstrated on the one-hand side by the N_e measured in Hall and on the other-hand side by the absorptance of the layers for wavelengths greater than 1000 nm, where free carrier absorption occurs. The increasing absorptance, which correlates well with an increasing N_e, results from photon interactions with free charge carriers. Films prepared with an ArO_2 flow of 8 sccm, exhibiting the lowest N_e of 0.6×10^{20} cm^{-3}, also showed the lowest absorptance in that range. In contrast, films prepared with 3.6 sccm ArO_2 or less, with N_e of up to 1.5×10^{20} cm^{-3}, demonstrated the highest absorptance. These observations strongly suggest that the number of free charge carriers in SnO_x films directly depends on the oxygen content in the process gas.

Besides the change in absorption in the NIR, there is also a visible influence of the ArO_2 flow on the absorptance for wavelengths $<$800 nm. Although a reduction in E_g of 0.1 eV can be observed for ArO_2 fluxes of 6 and 8 sccm, the most significant change in this range appears to correlate primarily with the change in sub-band gap absorption. We first attempted to quantify this absorption using the Urbach tail approximation, which assumes that sub-gap absorption follows an exponential shape. The formation of such an exponential absorption tail, also known as the Urbach tail, is associated with phenomena such as structural disorder (defect density, grain boundaries, or lattice strain), ionized impurities, and phonon-charge carrier interactions.[1,23] Using this method, values for E_U as high as 620–860 meV were calculated for films with the highest N_e of ≈ 1.3–1.5×10^{20} cm^{-3}, while values for E_U of $<$200 meV were calculated for films fabricated at high ArO_2 flow rates with lower values for N_e of 0.7×10^{20} cm^{-3} and less, which would indicate that the concentration of ionized impurities potentially significantly impacts E_U. However, despite the observed reduction in E_U for higher ArO_2 flow rates, no increase in μ_H can be observed, which would be expected if ionized impurities are reduced. μ_H depends on electron scattering events, like scattering at ionized impurities or structural disorder, which results in the reduction of μ_H.[24,25] Interestingly, despite the reduction in E_U, which equates to a reduction of film disorder, μ_H is also reduced. However, a closer look at the absorption within the band gap of films fabricated at ArO_2 flows below 6 sccm reveals that it does not follow the typical exponential behavior characteristic of Urbach tails. In the semi-logarithmic plot of the absorption coefficient, which for classical Urbach tails should exhibit a linear region within the bandgap—allowing the Urbach energy to be determined from its slope—regions with varying slopes appear instead (see Figure S1a,b, Supporting Information). This suggests that there is not a single dominant absorption process associated with, for example, disorder, but rather a combination of effects. We, therefore, ask ourselves whether the Urbach approximation approach to quantifying sub-gap absorption is valid at all or whether we are extremely overestimating the actual Urbach tails. The multiple slopes could hint at the presence of absorption peaks within the bandgap. These potential absorption peaks disappear at an ArO_2 flow of 6 sccm and more, which led to a significant drop in the calculated values for E_U from $\approx$700 meV at 5 sccm ArO_2 flow to less than 200 meV at 6 sccm. Such absorption peaks could originate, for example, from localized states, which may be caused by defects such as oxygen vacancies or interstitials introducing discrete electronic states within the band gap or from the overlap of different band gaps within the film. However, as discussed above, one would expect that the disappearance of scattering centers, such as localized defects, would lead to a significant increase in μ_H. We, therefore, suspect that the sub-gap absorption could rather be explained by the overlap of different band gaps. Such overlap could arise from the mixing of different structures, such as amorphous and crystalline regions, or from the presence of a secondary phase with a smaller band gap in the film.[16,26] XRD measurements (see Figure S1, Supporting Information) of unheated films at 3.4, 5, and 8 sccm ArO_2 flow rates reveal that all films are amorphous, which gives no indication of crystallization for layers fabricated at higher oxygen flow rates. Therefore, it is noteworthy that these changes, besides the reduction in ionized impurities, may be explained by an oxygen content-dependent transition from a mixed phase of SnO (tin(II) oxide) and SnO_2 (tin(IV) oxide) to a SnO_2-like film at high ArO_2 flow rates and which impacts charge carrier donors (see **Table 4**).[16,27] Similar observations were made by Koida et al.[16] Interestingly, both N_e and μ_H decrease simultaneously

Table 4. SnO_x phase, oxidation states of Sn and coordination number.

	Description	Oxidation state	Coordination number
Increasing O_2 ↓	SnO (tin(II) oxide)	Sn^{2+}	4
	oxygen-deficient SnO_2 (tin(IV) oxide), undercoordinated due to missing oxygen atoms[33]	Sn^{4+}	4
	SnO_2 (tin(IV) oxide), fully coordinated[33]	Sn^{4+}	6

© 2025 The Author(s). physica status solidi (RRL) Rapid Research Letters published by Wiley-VCH GmbH
18626270, 0, Downloaded from https://onlinelibrary.wiley.com/doi/10.1002/pssr.202400404 by Helmholtz-Zentrum Berlin Für, Wiley Online Library on [02/03/2025]. See the Terms and Conditions (https://onlinelibrary.wiley.com/terms-and-conditions) on Wiley Online Library for rules of use; OA articles are governed by the applicable Creative Commons License

with the reduction in calculated alleged E_U, suggesting a direct correlation. This indicates that the secondary phase may contribute not only optically but also electrically, potentially acting as a charge carrier donor. When the sub-gap absorption transitions from multiple slopes to an exponential decay, N_e decreases, resulting in a decline in μ_H. In amorphous materials with low N_e, charge carrier transport is often limited due to carrier trapping in localized states, which results in a carrier movement described by hopping.[28] At higher charge carrier densities, the Fermi level shifts upward, partially filling these states and reducing their impact on carrier transport. As a result, free carriers can move more efficiently at sufficiently high densities without being significantly hindered by trapping effects. However, to investigate this relationship in more detail, further measurements such as Rutherford backscattering spectrometry would be necessary, which determines the film's atomic density and composition, i.e., the O/Sn ratio, and which goes beyond the scope of the letter.

None of the temperature treatments caused the SnO_x films to crystallize. In the literature, crystallization is reported for temperatures of 400 °C and higher, while an amorphous structure is retained up to 300 °C.[19,27] Post-deposition annealing had varying effects on the films. In this experiment, neither the 130 °C nor the 210 °C post-annealing treatment increased charge carrier density. As opposed to the results by Koida et al. where post-annealing at 200 °C led to an increased charge carrier density for their RPD SnO_x,[16] we, instead, observed a slight reduction in N_e, from 1.5×10^{20} cm^{-3} (as-deposited) to 1.4×10^{20} cm^{-3} after annealing at either temperature. This is corroborated by lower absorption in the long-wavelength range, which reflects reduced free carrier absorption. One explanation for this could be that some undercoordinated Sn atoms increase their coordination number by filling missing oxygen atom sites with oxygen from the atmosphere during post-annealing, as explained in Table 4. μ_H exhibited only minor changes with post-annealing. Post-annealing at 130 °C slightly increased mobility to 8.9 cm^2 Vs^{-1}, potentially due to the healing of film defects or the deactivation of oxygen vacancies (ionized impurities). However, annealing at 210 °C notably reduced μ_H to 6.7 cm^2 Vs^{-1}, again.

Pre-treatment of the substrate at 150 °C before deposition for 10 min significantly increased μ_H to 10.1 cm^2 Vs^{-1} compared to films without pre-treatment. This improvement likely results from enhanced substrate surface diffusion of sputtered atoms during deposition due to the preheated substrate, facilitating improved film growth conditions.[29,30] A combination of pre- and post-heating yielded the lowest ρ of this study by achieving the highest N_e of 1.7×10^{20} cm^{-3} paired with the highest μ_H of 11.1 cm^2 Vs^{-1}. Interestingly, others reported highest values in their study of μ_H and N_e for SnO_x sputter deposited at room temperature, while applying a substrate temperature of 100 °C or more during the sputter deposition would lead to reduced values and increased resistivity of their films, for which they also reported the onset of crystallinity.[18,31,32] The difference to this work is, however, that these depositions were reactive, which might lead to fundamentally different growth conditions. When looking at the absorption coefficient in Figure 3c) it seems like none of the heat treatments have a major impact on the structure of the films. While small changes in the slope can be observed Figure 2d), the different temperature treatments do not significantly impact on the overall absorption behavior within the band gap. However, in order to replace indium-based TCOs such as IZO or ITO in optoelectronic applications, the ρ of these SnO_x layers must be reduced even further. These commonly used TCOs yield ρ of 1 mΩ cm and less.[1] The lowest ρ of this study was 3.4 mΩ cm, achieved by "in-situ" pre- and post-heating at 3.4 sccm ArO_2 flow rate, which is still more than eight times as high as the presented ρ of IZO, due to the lower N_e and μ_H. Nonetheless, the results of this study give a promising outlook on the effectiveness of heating during the deposition process. Depending on the limits set by the substrate, it can be assumed that the ρ of the SnO_x layers can be reduced even further with an optimized heating process.

4. Conclusion

Our study demonstrates that the optoelectronic properties of SnO_x films produced via RF magnetron sputtering with a ceramic target strongly depend on the amount of oxygen added to the process gas. Without intentional heating or post-deposition annealing, we were able to fabricate a SnO_x film with a sheet resistance of 5.3 mΩ cm, a carrier concentration of 1.5×10^{20} cm^{-3}, and a carrier mobility of 7.7 cm^2 Vs^{-1}. However, this layer exhibits significant absorption in the visible range for wavelengths below 800 nm, likely due to a secondary phase (SnO) within the film, which has a smaller optical bandgap. We hypothesized that films produced in our experiments with ArO_2 fluxes below 6 sccm consist of a mixed-phase structure containing SnO_2 and SnO-like regions. Furthermore, we believe that the secondary phase also has an electrical contribution, as both charge carrier density and mobility decrease when the sub-gap absorption vanishes. By applying pre- and post-treatment at 150 °C in the sputtering chamber, we further reduced the sheet resistance to 3.4 mΩ cm by increasing both the carrier density to 1.7×10^{20} cm^{-3} and the carrier mobility to 11.1 cm^2 Vs^{-1}. To the best of our knowledge, this carrier concentration represents the highest reported value for a SnO_x layer produced by magnetron sputtering.

Supporting Information

Supporting Information is available from the Wiley Online Library or from the author.

Acknowledgements

This work was funded by the German Federal Ministry for Economic Affairs and Climate Action (BMWK) through the KOALA-PLUS project (grant no. 03EE1109A).

Open Access funding enabled and organized by Projekt DEAL.

Conflict of Interest

The authors declare no conflict of interest.

© 2025 The Author(s). physica status solidi (RRL) Rapid Research Letters published by Wiley-VCH GmbH

18626270, 0, Downloaded from https://onlinelibrary.wiley.com/doi/10.1002/pssr.202400404 by Helmholtz-Zentrum Berlin Für, Wiley Online Library on [02/03/2025]. See the Terms and Conditions (https://onlinelibrary.wiley.com/terms-and-conditions) on Wiley Online Library for rules of use; OA articles are governed by the applicable Creative Commons License

Author Contributions

Marlene Härtel: conceptualization (equal); formal analysis (lead); investigation (equal); writing—original draft (lead). **Angelika Harter**: writing—original draft (supporting); writing—review & editing (supporting). **Darja Erfurt**: conceptualization (equal); formal analysis (supporting); investigation (equal). **Reiner Klenk**: investigation (supporting); writing—review & editing (supporting). **Alexander Steigert**: formal analysis (supporting); writing—review & editing (supporting). **Lars Korte**: supervision (supporting). **Rutger Schlatmann**: funding acquisition (equal). **Bernd Stannowski**: funding acquisition (lead); project administration (lead); supervision (equal); writing—review & editing (supporting).

Data Availability Statement

The data that support the findings of this study are available from the corresponding author upon reasonable request.

Keywords

indium-free, solar cells, sputter deposition, tin oxide (SnO_x), transparent conductive oxides

Received: December 16, 2024
Revised: February 5, 2025
Published online:

[1] M. Morales-Masis, S. Martin De Nicolas, J. Holovsky, S. De Wolf, C. Ballif, *IEEE J. Photovoltaics* **2015**, *5*, 1340.
[2] Y. Zhang, M. Kim, L. Wang, P. Verlinden, B. Hallam, *Energy Environ. Sci* **2021**, *14*, 5587.
[3] M. Batzill, U. Diebold, *Prog. Surf. Sci.* **2005**, *79*, 47.
[4] G. K. Dalapati, H. Sharma, A. Guchhait, N. Chakrabarty, P. Bamola, Q. Liu, G. Saianand, A. M. Sai Krishna, S. Mukhopadhyay, A. Dey, T. K. S. Wong, S. Zhuk, S. Ghosh, S. Chakrabortty, C. Mahata, S. Biring, A. Kumar, C. S. Ribeiro, S. Ramakrishna, A. K. Chakraborty, S. Krishnamurthy, P. Sonar, M. Sharma, *J. Mater. Chem. A* **2021**, *9*, 16621.
[5] J. A. Raiford, C. C. Boyd, A. F. Palmstrom, E. J. Wolf, B. A. Fearon, J. J. Berry, M. D. McGehee, S. F. Bent, *Adv. Energy Mater.* **2019**, *9*, 1902353.
[6] A. F. Palmstrom, J. A. Raiford, R. Prasanna, K. A. Bush, M. Sponseller, R. Cheacharoen, M. C. Minichetti, D. S. Bergsman, T. Leijtens, H. P. Wang, V. Bulović, M. D. McGehee, S. F. Bent, *Adv. Energy Mater.* **2018**, *8*, 1800591.
[7] D. Gao, B. Li, Q. Liu, C. Zhang, Z. Yu, S. Li, J. Gong, L. Qian, F. Vanin, K. Schutt, M. A. Davis, A. F. Palmstrom, S. P. Harvey, N. J. Long, J. M. Luther, X. C. Zeng, Z. Zhu, *Science* **2024**, *386*, 187.
[8] L. Qiu, Z. Liu, L. K. Ono, Y. Jiang, D. Y. Son, Z. Hawash, S. He, Y. Qi, *Adv. Funct. Mater.* **2019**, *29*, 1806779.
[9] G. Bai, Z. Wu, J. Li, T. Bu, W. Li, W. Li, F. Huang, *Sol. Energy* **2019**, *183*, 306.
[10] S. Lan, W. Zheng, S. Yoon, H. U. Hwang, J. W. Kim, D. Kang, J. Lee, H. Kim, *ACS Appl. Energy Mater.* **2022**, *5*, 14901.
[11] F. Ali, N. D. Pham, H. J. Bradford, N. Khoshsirat, K. Ostrikov, J. M. Bell, H. Wang, T. Tesfamichael, *ChemSusChem* **2018**, *11*, 3096.
[12] C. Yu, Q. Zou, Q. Wang, Y. Y. Zhao, X. Ran, G. Dong, C. W. Peng, V. Allen, X. Cao, J. Zhou, Y. Y. Zhao, X. Zhang, *Nat. Energy* **2023**, *8*, 1119.
[13] Y. Zakaria, B. Aïssa, T. Fix, S. Ahzi, A. Samara, S. Mansour, A. Slaoui, *Sci. Rep.* **2022**, *12*, 15294.
[14] K. P. S. Zanoni, D. Pérez-del-Rey, C. Dreessen, N. Rodkey, M. Sessolo, W. Soltanpoor, M. Morales-Masis, H. J. Bolink, *ACS Appl. Mater. Interfaces* **2023**, *15*, 32621.
[15] W. Soltanpoor, A. E. A. Bracesco, N. Rodkey, M. Creatore, M. Morales-masis, *Sol. Cells* **2023**, *7*, 2300616.
[16] T. Koida, J. Nomoto, *Chem. Mater.* **2024**, *36*, 6838.
[17] E. Rucavado, Q. Jeangros, D. F. Urban, J. Holovský, Z. Remes, M. Duchamp, F. Landucci, R. E. Dunin-Borkowski, W. Körner, C. Elsässer, A. Hessler-Wyser, M. Morales-Masis, C. Ballif, *Phys. Rev. B* **2017**, *95*, 245204.
[18] Y. Tao, B. Zhu, Y. Yang, J. Wu, X. Shi, *Mater. Chem. Phys.* **2020**, *250*, 123129.
[19] D. S. Ginley, H. Hosono, D. C. Paine, *Handbook of Transparent Conductors*, Springer, New York, **2010**, pp. 153–160.
[20] M. Haghighi, N. Ghazyani, S. Mahmoodpour, R. Keshtmand, A. Ghaffari, H. Luo, R. Mohammadpour, N. Taghavinia, M. Abdi-Jalebi, *Sol. RRL* **2023**, *7*, 220108.
[21] B. Demaurex, S. De Wolf, A. Descoeudres, Z. Charles Holman, C. Ballif, *Appl. Phys. Lett.* **2012**, *101*, 171604.
[22] S. De Wolf, M. Kondo, *J. Appl. Phys.* **2009**, *105*, 103707.
[23] S. Schönau, F. Ruske, S. Neubert, B. Rech, *Appl. Phys. Lett.* **2013**, *103*, 192108.
[24] R. Martins, P. Barquinha, A. Pimentel, L. Pereira, E. Fortunato, *Phys. Status Solidi Appl. Mater. Sci.* **2005**, *202*, 95.
[25] T. Koida, M. Kondo, K. Tsutsumi, A. Sakaguchi, M. Suzuki, H. Fujiwara, *J. Appl. Phys.* **2010**, *107*, 033514.
[26] K. Ellmer, R. Mientus, *Thin Solid Films* **2008**, *516*, 5829.
[27] Y. Porte, R. Maller, H. Faber, H. N. AlShareef, T. D. Anthopoulos, M. A. McLachlan, *J. Mater. Chem. C* **2016**, *4*, 758.
[28] A. J. Leenheer, J. D. Perkins, M. F. A. M. Van Hest, J. J. Berry, R. P. O'Hayre, D. S. Ginley, *Phys. Rev. B* **2008**, *77*, 115215.
[29] K. Ellmer, T. Welzel, *J. Mater. Res.* **2012**, *27*, 765.
[30] J. A. Thornton, *Annu. Rev. Mater. Sci.* **1977**, *7*, 239.
[31] W. Belayachi, G. Ferblantier, T. Fix, G. Schmerber, J. L. Rehspringer, T. Heiser, A. Slaoui, M. Abd-Lefdil, A. Dinia, *ACS Appl. Energy Mater.* **2022**, *5*, 170.
[32] S. E. K. Kim, M. Oliver, *Met. Mater. Int.* **2010**, *16*, 441.
[33] S. Kiyohara, D. Mora-fonz, A. Shluger, Y. Kumagai, F. Oba, *J. Phys. Chem. C* **2022**, *126*, 18833.

© 2025 The Author(s). physica status solidi (RRL) Rapid Research Letters published by Wiley-VCH GmbH

18626270, 0, Downloaded from https://onlinelibrary.wiley.com/doi/10.1002/pssr.202400404 by Helmholtz-Zentrum Berlin Für, Wiley Online Library on [02/03/2025]. See the Terms and Conditions (https://onlinelibrary.wiley.com/terms-and-conditions) on Wiley Online Library for rules of use; OA articles are governed by the applicable Creative Commons License